Journal of Biomedical Optics

SPIEDigitalLibrary.org/jbo

Multiphoton microscopy and microspectroscopy for diagnostics of inflammatory and neoplastic lung

Ina Pavlova
Kelly R. Hume
Stephanie A. Yazinski
James Flanders
Teresa L. Southard
Robert S. Weiss
Watt W. Webb

SPIE

Multiphoton microscopy and microspectroscopy for diagnostics of inflammatory and neoplastic lung

Ina Pavlova,[a,†] Kelly R. Hume,[b,*,†] Stephanie A. Yazinski,[b] James Flanders,[c] Teresa L. Southard,[b,d] Robert S. Weiss,[b] and Watt W. Webb[a]
[a]Cornell University, School of Applied and Engineering Physics, Ithaca, New York
[b]Cornell University, Department of Biomedical Sciences, Ithaca, New York
[c]Cornell University, Cornell University Hospital for Animals, Department of Clinical Sciences, College of Veterinary Medicine, Ithaca, New York
[d]College of Veterinary Medicine, Section of Pathology, Ithaca, New York

Abstract. Limitations of current medical procedures for detecting early lung cancers inspire the need for new diagnostic imaging modalities for the direct microscopic visualization of lung nodules. Multiphoton microscopy (MPM) provides for subcellular resolution imaging of intrinsic fluorescence from unprocessed tissue with minimal optical attenuation and photodamage. We demonstrate that MPM detects morphological and spectral features of lung tissue and differentiates between normal, inflammatory and neoplastic lung. *Ex vivo* MPM imaging of intrinsic two-photon excited fluorescence was performed on mouse and canine neoplastic, inflammatory and tumor-free lung sites. Results showed that MPM detected microanatomical differences between tumor-free and neoplastic lung tissue similar to standard histopathology but without the need for tissue processing. Furthermore, inflammatory sites displayed a distinct red-shifted fluorescence compared to neoplasms in both mouse and canine lung, and adenocarcinomas displayed a less pronounced fluorescence emission in the 500 to 550 nm region compared to adenomas in mouse models of lung cancer. These spectral distinctions were also confirmed by two-photon excited fluorescence microspectroscopy. We demonstrate the feasibility of applying MPM imaging of intrinsic fluorescence for the differentiation of lung neoplasms, inflammatory and tumor-free lung, which motivates the application of multiphoton endoscopy for the *in situ* imaging of lung nodules. [DOI: 10.1117/1.JBO.17.3.036014]

Keywords: multiphoton microscopy; endoscopy; lung cancer; minimally invasive diagnostics; mouse models for lung adenocarcinoma.

Paper 11494 received Sep. 8, 2011; revised manuscript received Jan. 23, 2012; accepted for publication Jan. 24, 2012; published online Apr. 5, 2012.

1 Introduction

Lung cancer is the deadliest malignancy in the US and worldwide.[1] Despite advances in medical imaging, the five-year survival rate has remained low because most lung cancer cases are presently diagnosed at locally advanced or metastatic stages of disease.[1] Clinical studies have recently shown that screening asymptomatic smokers for lung cancer leads to detecting tumors at an earlier and therefore more curable stage of disease.[2,3] Although improvements in medical imaging allow detection of smaller nodules, direct and minimally invasive diagnosis of these nodules could reduce the number of unnecessary biopsies and follow-up procedures. This suggested the need for new imaging approaches that provide high-resolution interrogation in real-time and accurately distinguish malignant nodules from other disease states. Here, we evaluate the applicability of multiphoton microscopy (MPM) for visualizing lung disease by determining the two-photon excited endogenous fluorescence and second harmonic generation (SHG) of *ex vivo* lung using mouse models of lung cancer and by suggesting potential MPM detected criteria for the classification of lung lesions.

A variety of optical imaging modalities have been implemented as endoscopic devices for *in vivo* detection of neoplasias in internal organs.[4–7] In the lungs, wide-field autofluorescence bronchoscopes have already been tested clinically for the detection of early bronchial tumors,[8] and confocal microendoscopes have been applied for the *in vivo* imaging of alveolar ducts.[9] Here, we introduce MPM as a potential imaging modality for diagnostic visualization of lung neoplasms.

MPM is one of the preferred microscopy modalities for subcellular resolution imaging of optically scattering tissue due to the deeper penetration depth and the minimized photodamage of the near-infrared excitation light.[10–12] Intrinsic two-photon excited fluorescence and SHG from tissue provide subcellular resolution images with sufficient morphological details to be diagnostically useful, as has been demonstrated with unprocessed biopsies from human urinary bladder,[13] ovary,[14] gastrointestinal tract,[15] and prostate samples.[16] Similar to the established diagnostic methods of histopathology, the endogenous fluorescence and SHG captured by MPM images provide information about the tissue architecture of the interrogated site. MPM also allows the visualization of intrinsic fluorescence patterns on a cellular level and changes in fluorescence emission as tissues develop abnormalities. Common cellular fluorophores in unprocessed tissue include intrinsic metabolic indicators such as NADH and flavins.[12,17,18] Extracellular endogenous signals in MPM images originate from structural fibers

*Current Affiliation: Department of Clinical Sciences, College of Veterinary Medicine, Cornell University, Ithaca, New York.
†These authors contributed equally.

Address all correspondence to: Watt Wetmore Webb, Cornell University, School of Applied and Engineering Physics, Clark Hall 223, Ithaca, New York. Tel: +607 255 3331; Fax: +607 255 7658; E-mail: www2@cornell.edu

0091-3286/2012/$25.00 © 2012 SPIE

such as collagen and elastin.[12] SHG from collagen is unique to MPM imaging and has been used to monitor changes in collagen composition due to tumor development that were not obvious by standard histopathology.[19] Therefore, multiphoton excitation microscopy has the potential to visualize both microanatomical and spectral properties without the need for tissue processing.

The respiratory lung consists of alveolar ducts with numerous alveoli that are lined by a layer of flattened epithelial cells and by a septum with alveolar capillaries, as well as elastin and collagen fibers.[20] Previous MPM studies have shown that endogenous signal from normal human[21] and mouse[22] lung originates predominantly from the alveolar septa of intact alveoli, with collagen fibers emitting SHG at half the excitation wavelength, and elastin fibers having a broad endogenous fluorescence in the green emission region. Lung adenocarcinoma, the most common type of human lung cancer, is believed to form in some cases after progressive pathological changes and to arise from a preinvasive lesion of atypical epithelial cells called atypical adenomatous hyperplasia (AAH).[23] In contrast to the normal lung parenchyma, adenocarcinomas are characterized as cellular masses with diverse histopathology that distort the fibrous alveolar network.[24]

We evaluated the two-photon excited endogenous fluorescence and SHG of unprocessed normal, preneoplastic and neoplastic lung in two different mouse lung cancer models. We imaged unprocessed lungs from a mouse model of lung adenocarcinoma based on the conditional expression of the oncogene K-ras that genetically mimics human lung adenocarcinoma and allows investigation of lesions at well defined and predictable (including early) stages of tumor progression.[25] In this model, targeted delivery of Cre recombinase activates the expression of a conditional K-ras allele (LSL-K-ras G12D) in scattered cells throughout the lungs, resulting in precursor lesions, such as AAH, that progress to adenomas and adenocarcinomas in a reproducible, temporal sequence. We also imaged lung from a second mouse model based on transgenic overexpression of Rrm2, a subunit of the enzyme ribonucleotide reductase (RNR) that is a key regulator of *de novo* nucleotide biosynthesis.[26] Tumorigenesis in Rrm2 overexpressing transgenic ($Rrm2^{Tg}$) mice involves a mutagenic mechanism that recapitulates the stochastic nature of tumor development in humans and results in lesions with histopathological resemblance to human lung neoplasms. Furthermore, we confirmed diverse applicability of our findings in a case of spontaneously occurring canine lung cancer. This proof-of-principle study of mouse and dog lung neoplasms demonstrates the potential of MPM as an imaging technique for lung nodules, and provides clear motivation for MPM applications for *in vivo* evaluation of lung cancer, particularly by endoscopy.

2 Materials and Methods

2.1 *Mouse Models of Lung Adenocarcinoma*

LSL-K-ras G12D mice[25] were obtained from the Mouse Models of Human Cancer Consortium and backcrossed either onto a pure 129SvEv or onto an FVB/N genetic background. To induce Cre-mediated recombination and K-ras G12D activation in the lungs, adult mice were anesthetized with 2.5% Avertin (tribromoethanol and tert-amyl alcohol) and were administered 6.7×10^8 plaque-forming units (PFU) of Ad-Cre virus, diluted in 40 μl of phosphate buffered saline (PBS), either intratracheally or intranasally. Note that 1 : 10, 1 : 100 or 1 : 1000 dilutions were used for some mice. The lungs were harvested 6 to 20 weeks post infection from euthanized mice. $Rrm2^{Tg}$ mice were maintained on pure FVB/N genetic background as previously described.[26] All animal housing and experimentation was performed in accordance with institutional animal care and use guidelines.

2.2 *Lung Tissue Processing and Histopathological Assessment*

Mice were euthanized by carbon dioxide asphyxiation. The lung lobes were removed and visually inspected for abnormalities. Normal lung has a uniform pink color throughout the surface of the lobes, whereas regions with potential abnormalities appear as white or red discolorations in the smooth surface of the lung. Sites with abnormal appearance were selected on each lobe and imaged within two hours after euthanasia. All lobes were kept in chilled PBS until imaging. Immediately after imaging, the lobes were fixed in 10% buffered formalin or 4% paraformaldehyde. H&E stained sections were prepared from each lobe following standard embedding and staining protocols. H&E sections (~6 μm thick) were obtained from a similar depth and location within samples to that imaged by MPM. Low-magnification micrographs were obtained for each H&E section and compared to a low-magnification MPM image of the lobe prior to tissue fixation. Using structural features present on both the H&E and MPM image, the location of the site imaged at high-magnification MPM was approximated on the H&E section. Thus, histopathological assessment was performed at a site on the H&E section comparable to the site imaged with MPM prior to tissue processing. Pathological assessment was performed according to guidelines in the Mouse Models of Human Cancers Consortium.[27]

Lung samples were also obtained from a 12-year-old female spayed Miniature Poodle treated at the Cornell University Hospital for Animals for bronchioloalveolar carcinoma of the left caudal lung lobe. The left caudal lung lobe was removed by standard lung lobectomy by a veterinary surgeon. Clinically abnormal and normal samples were obtained from the resected lobe by a veterinary oncologist. Prior to surgery, an informed consent form was signed by the owner of the dog. The samples were kept in chilled PBS for about two hours prior to imaging. Similar tissue imaging and processing were followed as for mouse lungs.

2.3 *MPM of Unprocessed Lung Tissue*

Imaging was performed with a commercial multiphoton microscope (Olympus Fluoview® FV1000MPE, Olympus America Inc, Center Valley, PA) at a shorter (760 nm) and longer (860 nm) excitation. An Olympus 25×, 1.05 NA water immersion objective was used and all images were obtained with ~23 mW (at 760 nm excitation) and ~25 mW (at 860 nm excitation) average power at the objective, pixel dwell time of 2 μs and at 1.1 sec /frame. Displayed MPM images represent a Kalman average of three frames. Autofluorescence and SHG were captured by three detection channels, equipped with multi-alkali photomultiplier tubes. The first channel detected signal at 420 to 460 nm, the second and third channels captured endogenous fluorescence at 500 to 550 nm and at 575 to 635 nm; respectively. Images from each channel were pseudocolored and superimposed. Displayed MPM images represent superimposed images: "green" pixels indicates fluorescence detected predominantly in the second channel, "red" indicates fluorescence detected predominantly in the third channel and "blue" indicates emission at 420 to 460 nm (including SHG at 860 nm excitation

only). The contrast and brightness were adjusted equally for all displayed MPM images at a particular excitation wavelength.

MPM was performed on lobes from eight control mice, including uninfected and Ad-Cre infected wild-type mice, and on lobes from 10 Ad-Cre infected LSL-K-ras G12D mice and two tumor bearing $Rrm2^{Tg}$ mice. Images were taken from 1 to 4 sites per lobe. Unaffected lobes with normal appearance were imaged approximately 20 to 30 μm below the pleura at a representative site. Lobes with grossly visible abnormalities were imaged at several sites ~20 to 30 μm below the pleura; an image was taken from the center of each nodule and the tissue surrounding the nodule. For larger or heterogeneous nodules, images were taken from different areas within the nodule. In total, images were obtained from eleven tumor free unaffected (normal) lung sites, four adenomas, six adenocarcinomas, three sites with focal inflammation and six regions with diffuse hyperplasia. MPM images from adenomas and adenocarcinomas were analyzed by determining the Green (500 to 550 nm)/Blue (420 to 460 nm) fluorescence emission ratio for each MPM image (defined as the average pixel intensity value from the green channel (500 to 550 nm) divided by the sum of the average pixel intensity values from the blue (420 to 460 nm) and green channel (500 to 550 nm). The ratio was calculated only for pixels within the nodule and not from the surrounding tissue.

2.4 *Two-Photon Excited Microspectroscopy of Unprocessed Lung Tissue*

Microspectroscopy was performed using a spectrograph (Andor Technology, South Windsor, CT, USA) coupled to the microscope with a multimode optical fiber. A spectroscopic EEM CCD (Andor Technology, South Windsor, CT, USA), attached to the spectrograph, was used in full vertical binning mode to measure spectra from the imaged sample. Spectra were obtained by scanning a zoomed in (73×73 μm^2) region within each MPM image for an exposure time of 1.18 sec and average power at the objective of ~23 mW (at 760 nm excitation) and ~25 mW (at 860 nm excitation). Spectra were obtained at ~20 to 30 μm below the pleura. No photodamage was observed in the zoomed-in regions after spectroscopic acquisition.

Microspectroscopy was performed on lesions with dense cellular aggregations such as adenomas, adenocarcinomas and focal inflammatory sites. During MPM imaging at 760 nm, regions within each tumor composed of cells with dominant fluorescence at 420 to 460 nm were visually selected. Next, three spectra were sampled from zoomed in (73×73 μm^2) areas within these preselected regions. In focal inflammatory sites, clusters of inflammatory cells with yellow appearance on MPM images were sampled. Spectra were also obtained from normal sites by sampling zoomed in regions of the alveolar septa from unaffected alveoli. All spectra were background subtracted, smoothed by a Savitzky-Golay filter (MATLAB), and normalized by the maximum intensity value in the 400 to 650 nm region prior to analysis.

3 Results

To elucidate the intrinsic fluorescence and SHG patterns of peripheral lung tissue at different pathological stages, we obtained MPM images and two-photon excited fluorescence spectra from tumor-free unaffected, inflammatory and hyperplasic lung sites and from lung tumors, such as adenomas and adenocarcinomas. Images were visually analyzed to suggest a set of structural and spectral features for MPM-guided differentiation of lung sites at different pathological stages.

3.1 *Two-Photon Excited Intrinsic Fluorescence Features of Tumor Free Peripheral Mouse Lung*

To demonstrate the ability of MPM to differentiate normal from diseased lung, *ex vivo* MPM was first performed on tumor-free unaffected peripheral lung [Figs. 1(a)–1(f)]. MPM images showed similar microanatomical features to histopathology, with intact alveolar spaces and clearly apparent septa. The thin layer of epithelial cells comprising the alveoli was not visualized by MPM, and the two-photon excited intrinsic emission appeared to originate from the alveolar septa, not the associated epithelium. At 760 nm excitation, the brightest fluorescence originated from granular structures; individual cells were not readily visualized. Two-photon excited fluorescence spectra of intact alveoli from eleven different tumor-free unaffected lung sites peaked at ~480 nm (data not shown), which differed from fluorescence of typical cellular fluorophores such as NADH and flavins.[12,17,18] At 860 nm excitation, fluorescence originated predominantly from fibers within the alveolar walls that appeared green in MPM images [Fig. 1(c)], indicating fluorescence detected at 500 to 550 nm. Some alveoli also displayed fibers with blue appearance in MPM images [Figs. 1(f) and 2(c)], probably caused by SHG at 430 nm from collagen fibers in the alveolar septa. Microanatomically, this signal correlates well with the collagen distribution in Masson's trichrome stained tumor-free peripheral lung [Fig. 2(a)], indicating that fibers with blue appearance at 860 nm represent collagen from the alveolar septa. Intact alveoli without a readily visualized cellular component were observed in MPM images from all tumor-free lung sites and used as an MPM-detected feature to differentiate tumor-free and diseased lung in this study (Table 1).

Next, we evaluated the two-photon excited fluorescence patterns in MPM images from lung sites with diffuse and focal inflammation [Figs. 1(g)–1(l)]. Sites with diffuse inflammation showed readily identifiable individual cells infiltrating the alveolar lumina, whereas focal inflammations appeared as denser cellular accumulations without clearly visualized borders. Histopathology indicated that the cellular infiltration in the diffuse inflammation site was caused by macrophages, whereas the focal inflammatory lesion was composed of lymphocytes and macrophages. The cells in both the diffuse and focal inflammation site appeared yellow in MPM images, indicating fluorescence detected at longer wavelengths (500 to 635 nm, channel 2 and 3). Furthermore, two-photon excited emission spectra from groups of cells within the focal inflammation showed a pronounced red-shifted emission at both 760 and 860 nm excitation [Figs. 3(a) and 3(b)]. Denser cellular accumulations with intrinsic fluorescence emission at longer wavelengths were observed in MPM images from all focal inflammation sites and used as an MPM-detected feature to differentiate focal inflammatory sites and neoplastic cellular masses in this study (Table 1). Infiltration of cells fluorescing at longer emission wavelengths was also observed in the lung parenchyma next to most of the adenocarcinomas. Histopathological assessment indicated that the alveoli next to most adenocarcinoma were filled with macrophages with eosinophilic cytoplasm.

3.2 *MPM of Diffuse Hyperplasia in Peripheral Mouse Lung*

Precursor lesions, such as AAH, in the LSL-K-ras G12D lung adenocarcinoma model were previously described as an

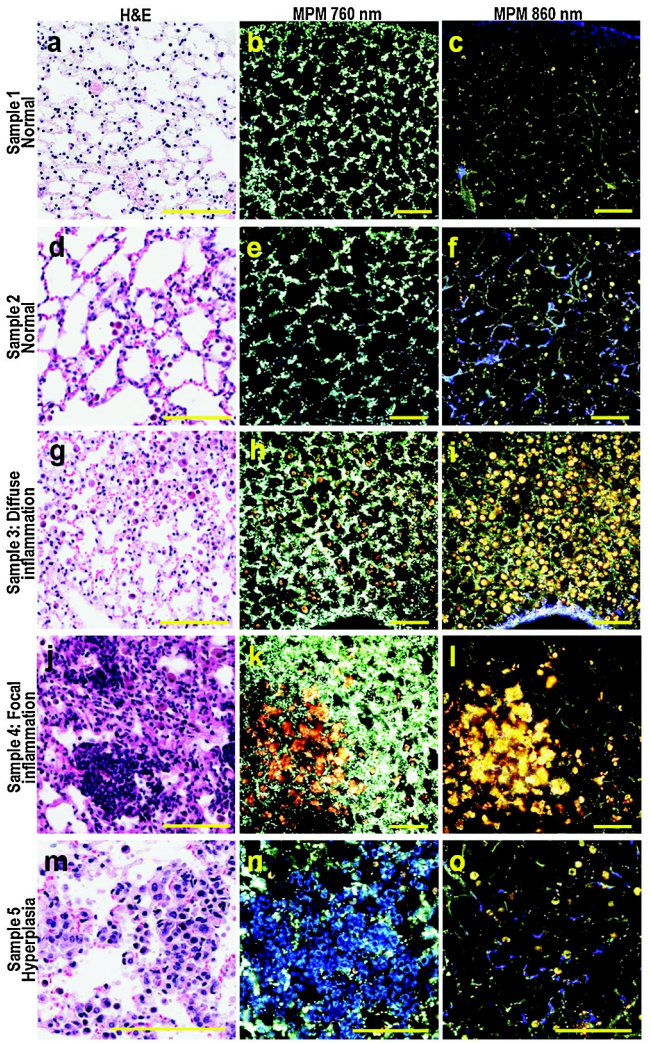

Fig. 1 Multiphoton microscopy (MPM)-detected intrinsic fluorescence characteristics of normal, inflammatory and hyperplasic peripheral mouse lung at shorter (760 nm) and longer (860 nm) wavelength excitation. (a–c), Images from an uninfected wild-type control mouse. H&E image displays normal lung parenchyma composed of alveolar spaces separated by thin septa. MPM images enable detection of intact alveolar spaces and septa and minimal cellular infiltration in the lumens. (d–f), Images from an Ad-Cre infected wild-type control mouse. H&E image displays normal lung parenchyma with a few small macrophages within alveolar spaces. (g–i), A site with diffuse inflammation. H&E image shows alveolar spaces with alveolar macrophages with intensely eosinophilic cytoplasm. MPM detects cells within alveolar lumina with yellow appearance, indicating fluorescence detected at 500 to 635 nm, channel 2 and 3. (j–l), A site with focal inflammation. H&E image shows perivascular spaces expanded by infiltrates of small lymphocytes, and alveolar spaces with eosinophilic macrophages. MPM detects cellular aggregates with bright fluorescence at detected at 500 to 635 nm. (m–o), A site with diffuse hyperplasia. H&E image shows accumulation of oval to cuboidal epithelial cells with no compression of the adjacent parenchyma. MPM imaging detects the accumulation of cells. At 760 nm excitation, these cells appear blue, indicating fluorescence detected predominantly at 420 to 460 nm, channel 1, while at 860 nm excitation they appear dim (fluorescence with very weak intensity). All samples were imaged before (MPM) and after (H&E) tissue processing. Scale bar: 100 μm.

accumulation of atypical epithelial cells on alveolar walls.[25] MPM images from peripheral lung with diffuse hyperplasia detected the accumulation of oval to cuboidal epithelial cells on alveolar walls (as confirmed by histopathology) without compression of the adjacent alveoli [Figs. 1(m)–1(o)]. At 760 nm excitation, these cells appeared blue in MPM images, indicating fluorescence detected predominantly at 420 to 460 nm. Furthermore, two-photon excited spectra from these cells displayed an emission peak at ~455 nm (data not shown), which is similar to emission maxima of spectra from the mouse tumors [Figs. 3(a) and 3(c)] and to values cited by previous publications on MPM of unprocessed tissue and attributed to cellular NADH.[17,18]

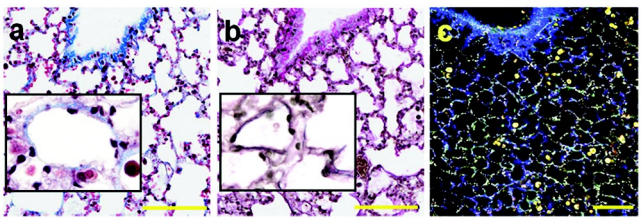

Fig. 2 Masson's trichrome (a), Verhoeff stain (b) and multiphoton microscopy (MPM) at 860 nm (c) of a tumor-free peripheral lung site comparing the location of collagen and elastin fibers in alveolar septa before (c) and after (a, b) tissue processing. Collagen fibers appear blue in (a), whereas elastin fibers appear black in (b). Inset: higher power view of collagen (a) and elastin (b) fibers. In the MPM image, fibers with dominant emission at 420 to 460 nm (blue color) are seen in the pleura and along alveolar septa. This signal is most likely due to SHG (at 430 nm) from collagen fibers. Note that the pattern of the collagen distribution shown in the Masson's trichrome image is very similar to the distribution fibers with blue color in the MPM image. Scale bar: 100 μm.

3.3 *MPM of Mouse Lung Neoplasms Such as Adenomas and Adenocarcinomas*

To elucidate the two-photon excited endogenous patterns of mouse lung neoplasms, we first imaged small adenomas (Fig. 4). In the H&E images, the adenomas appeared as well-demarcated nodules composed of neoplastic cuboidal epithelial cells that obliterated the alveolar spaces. MPM at 760 nm detected similar microanatomical patterns; the nodules appeared as dense cellular masses completely distorting the lung parenchyma, while the tissue immediately next to the nodule had intact alveoli. At 760 nm excitation, the majority of cells within the adenomas appeared blue in the MPM images, indicating fluorescence detected predominantly at 420 to 460 nm. Microspectroscopy confirmed that the two-photon excited fluorescence spectra from groups of cells within the adenomas peaked at ~455 nm [Figs. 3(a) and 3(c)]. Dense cellular aggregates with intrinsic fluorescence at 420 to 460 nm were observed in MPM images from all adenomas and described here as an MPM-detected feature (Table 1). At 860 nm excitation, the adenomas displayed an increased presence of fibers with dominant emission at 420 to 460 nm, as compared to the surrounding lung parenchyma [Figs. 4(c) and 4(f)]. This feature was visualized in three out of four adenomas. The adenoma that did not clearly display this feature was surrounded by lung parenchyma with diffuse hyperplasia.

MPM images from a mouse lung adenocarcinoma are shown in Fig. 5. At 760 nm excitation, most of the cells from a site within the tumor displayed dominant fluorescence emission at 420 to 460 nm, similar to the adenomas. More complex MPM patterns were observed at the periphery of the tumor [Fig. 5(h)] and the surrounding lung parenchyma [Fig. 5(k)] compared to the adenomas. In particular, the periphery of the lesion appeared to have cells with diverse structural and spectral

Table 1 Structural and spectral features observed in multiphoton microscopy (MPM) images of normal, inflammatory and neoplastic lung. The spectral features observed in MPM images were also supported by two-photon excited microspectroscopy. While standard histopathological criteria were used to diagnose the lung samples after tissue processing, the summarized features were based on observation of MPM images obtained from fresh, unprocessed tissue.

Groups	Structural features at 760 nm	Spectral features at 760 nm
Normal lung ($n = 11$)	Intact alveoli without a readily visualized cellular component	Intrinsic fluorescence from alveolar septa with emission peak ~480 nm
Focal inflammation ($n = 3$)	Cellular aggregations within alveolar lumens	Intrinsic cellular fluorescence at longer emission wavelengths (~500 to 635 nm)
Adenomas ($n = 4$)	Dense cellular masses that displace the lung parenchyma	Intrinsic cellular fluorescence predominantly at shorter emission wavelengths (~420 to 460 nm)
Carcinomas ($n = 6$)	Dense cellular masses that displace the lung parenchyma	Intrinsic cellular fluorescence predominantly at shorter emission wavelengths (~420 to 460 nm); less pronounced fluorescence at 500 to 550 nm (lower Green/Blue ratio) compared to adenomas.

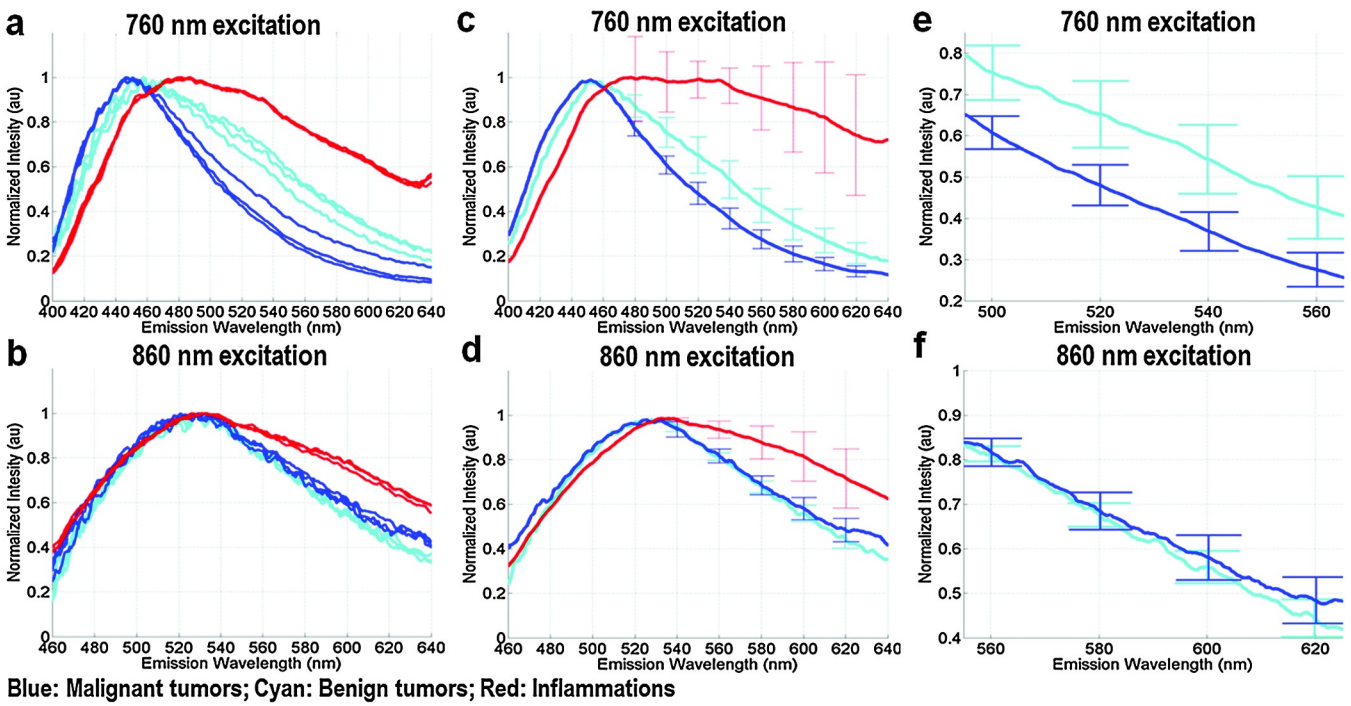

Fig. 3 Two-photon excited microspectroscopy illustrating differences in the intrinsic cellular fluorescence of mouse adenomas, adenocarcinomas and focal inflammations at shorter (760 nm) and longer (860 nm) wavelength excitation. (a–b), Representative spectra obtained from group of cells within an adenocarcinoma (blue lines), an adenoma (cyan lines) and a focal inflammation site (red lines). To display the spectral variation within each nodule, three separate spectra were recorded per site. All spectra were normalized by their maximum intensity value. (c–d), Average spectra from six different adenocarcinomas, four adenomas, and three focal inflammations. The error bars represent one standard deviation of the average fluorescence intensity values at emission wavelengths in the 400 to 620 nm region. (e–f), Selected emission wavelength region from the average spectra in (c) and (d) emphasizing that spectral differentiation between adenomas and adenocarcinomas is achieved at 760 nm and not 860 nm excitation.

patterns, while the surrounding lung parenchyma had marked infiltration of cells fluorescing at longer wavelengths. Histopathology confirmed the presence of focally extensive infiltrates of lymphocytes mixed with macrophages at the periphery of the lesion and marked macrophage infiltration in the surrounding alveoli. All adenocarcinomas in this study appeared as dense cellular masses in MPM images, and most of the cells within these masses displayed dominant cellular fluorescence emission at 420 to 460 nm. Therefore, the detection of cellular aggregates with dominant intrinsic fluorescence at 420 to 460 was described here as an MPM-detected characteristic of mouse adenocarcinomas (Table 1). At 860 nm excitation, the site within the adenocarcinoma [Fig. 5(f)] displayed more fibers with dominant emission at 420 to 460 nm, compared to the surrounding lung parenchyma [Fig. 5(l)]. Similar to the adenomas, this feature was detected by MPM at 860 nm in most (four out of six) adenocarcinomas and is likely to be SHG from collagen fibers at 430 nm. One of the adenocarcinomas that did not

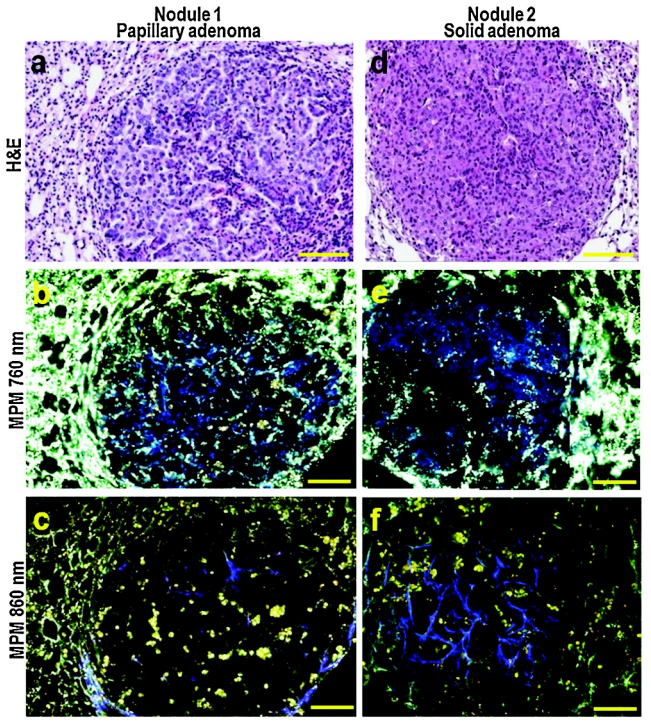

Fig. 4 Multiphoton microscopy (MPM)-detected intrinsic fluorescence characteristics of mouse adenomas (a type of benign lung tumor). (a–c), A papillary adenoma. The H&E image shows a well-demarcated nodule within the lung parenchyma composed of neoplastic cuboidal epithelial cells arranged in papillary projections. MPM at 760 nm shows a compact mass with cells, most of which have blue appearance (fluorescence detected at 420 to 460 nm). MPM at 860 nm enables the detection of more fibers with blue appearance within the mass compared to the surrounding alveoli. (d–f), A solid adenoma; the H&E image shows a well-demarcated nodule composed of neoplastic cuboidal cells, arranged in closely packed cords that obliterate the alveolar spaces. MPM detects similar patterns as (a–c). Scale bar: 100 μm.

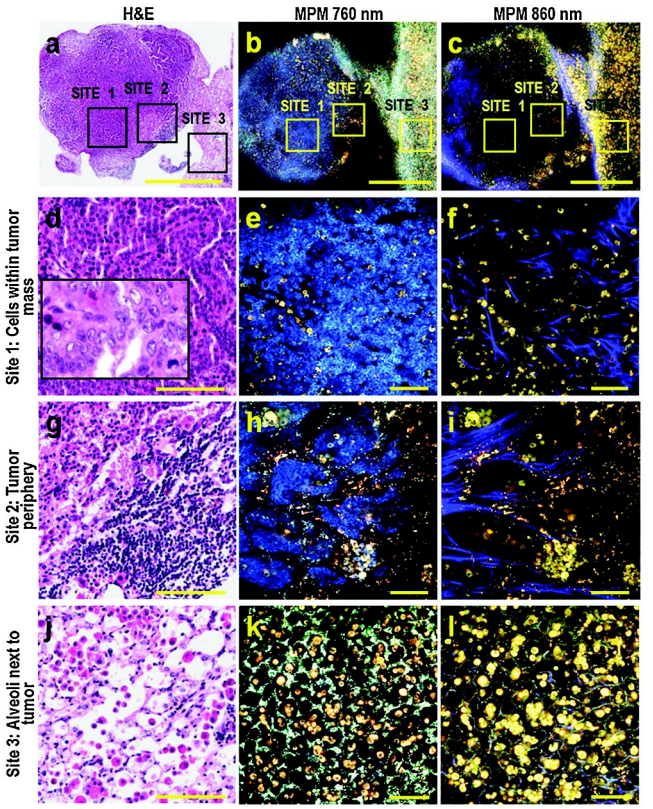

Fig. 5 Images of a mouse adenocarcinoma illustrating differences in multiphoton microscopy (MPM)-detected characteristics at sites within (site 1), at the periphery (site 2) and next to the tumor (site 3). (a–c), Low-magnification images indicating the approximate location of the sites displayed in (d–l). Histopathological assessment (a) reveals a well-demarcated, expansile neoplastic mass composed of epithelial cells that form papillary projections and solid areas and efface the pulmonary parenchyma. (d–f), A site within the tumor. Histopathologically (d), the mass consists of neoplastic cells with loss of nuclear polarity, variation in nuclear size and occasional mitotic figures (inset). MPM at 760 nm (e) detects a compact mass of cells; most of these cells appear blue (fluorescence detected at 420 to 460 nm, channel 1). (g–i), A site at the periphery of the tumor. The H&E shows focally extensive infiltrate of lymphocytes mixed with eosinophilic macrophages. MPM at 760 nm detects clusters of cells with different spectral patterns. (j–l), Lung parenchyma next to the mass. In the H&E image (j), the alveolar spaces are filled with numerous, variably-sized, eosinophilic macrophages. MPM at 760 nm detects cells with yellow appearance (fluorescence at 500 to 630 nm, channel 1 and 2) infiltrating the alveolar lumens. Scale bar: (a–c) 1000 μm, (d–l) 100 μm.

clearly display this feature was surrounded by lung parenchyma with diffuse hyperplasia. The biological basis for this feature has not been determined; however, advanced mouse lung adenocarcinomas are reported to deposit desmoplastic stroma around tumor cells[28] and the observed fiber accumulation by MPM could signify increased stromal (fibrous) deposition.

Visual observation of MPM images at 760 nm showed that most of the cells within the adenomas and adenocarcinomas displayed dominant fluorescence emission at 420 to 460 nm. However, quantitative analysis of the MPM images revealed that, compared to cells within adenomas, cells within the adenocarcinomas displayed lower fluorescence emission at 500 to 550 nm, relative to fluorescence emission at 420 to 460 nm. In particular, we calculated the Green (500 to 550 nm)/Blue (420 to 460 nm) emission ratio (the average pixel intensity from the 500 to 550 nm channel vs. the average pixel intensity from the 420 to 460 nm channel) from MPM images of all adenomas and (the central regions) of all adenocarcinomas. On average, at 760 nm excitation, the cells within adenocarcinomas displayed a Green (500 to 550 nm)/Blue (420 to 460 nm) ratio that was lower than the adenomas (ratio for adenocarcinomas: 0.38 ± 0.02, mean $\pm$ SD, $n = 6$; ratio for adenomas: 0.45 ± 0.04, mean $\pm$ SD, $n = 4$). This indicates that, for the current set of MPM images, cells within the malignancies displayed a less pronounced fluorescence at 500 to 550 nm (blue-shifted fluorescence) compared to the benign tumors.

3.4 *Spectroscopic Evaluation of Cells Within Mouse Lung Neoplasms and Focal Inflammatory Sites*

To further elucidate differences in cellular fluorescence patterns of lung neoplasms and focal inflammations, we collected two-photon excited spectra from groups of cells from an adenoma, adenocarcinoma and focal inflammation [Fig. 3(a)]. At 760 nm excitation, cells from the adenocarcinoma showed similar emission at 400 to 460 nm, but less pronounced spectral broadening at 500 to 600 nm, compared to those from the adenoma. Cells from the focal inflammation showed a marked red-shifted fluorescence compared to cells from either the adenoma or adenocarcinoma, especially at longer emission wavelengths (500 to 640 nm). To determine the degree of variations between samples, average two-photon excited emission spectra were

calculated from multiple samples for each histopathological category [Fig. 3(c)]. At 760 nm excitation, average spectra from the adenocarcinomas and adenomas showed similar cellular fluorescence at 400 to 460 nm, but different spectral emission at the 500 to 600 nm, confirming spectral trends observed from individual samples [Fig. 3(a)]. At 860 nm excitation, spectra from adenomas and adenocarcinomas displayed a similar emission peak and shape, whereas spectra from focal inflammations displayed a distinct red-shifted spectral broadening compared to all other categories. Spectroscopic trends summarized in Fig. 3 demonstrate that for the current data set, spectral differentiation between adenomas and adenocarcinomas was best achieved at 760 nm (and not at 860 nm) excitation and at 500 to 600 nm emission. However, focal inflammations were spectrally differentiated from lung neoplasms at both 760 and 860 nm excitation.

3.4.1 *MPM of canine lung carcinoma*

To confirm that our results were reproducible in spontaneously occurring lung carcinomas and applicable to larger mammals, we imaged normal and diseased lung tissue from a dog treated at Cornell University Hospital for Animals for bronchioloalveolar carcinoma of the left caudal lung lobe (Fig. 6). MPM images from an abnormal region with bronchioloalveolar carcinoma showed similar microanatomy to the H&E images, with cellular projections completely displacing the lung parenchyma. At 760 nm excitation, the cellular projections appeared blue in

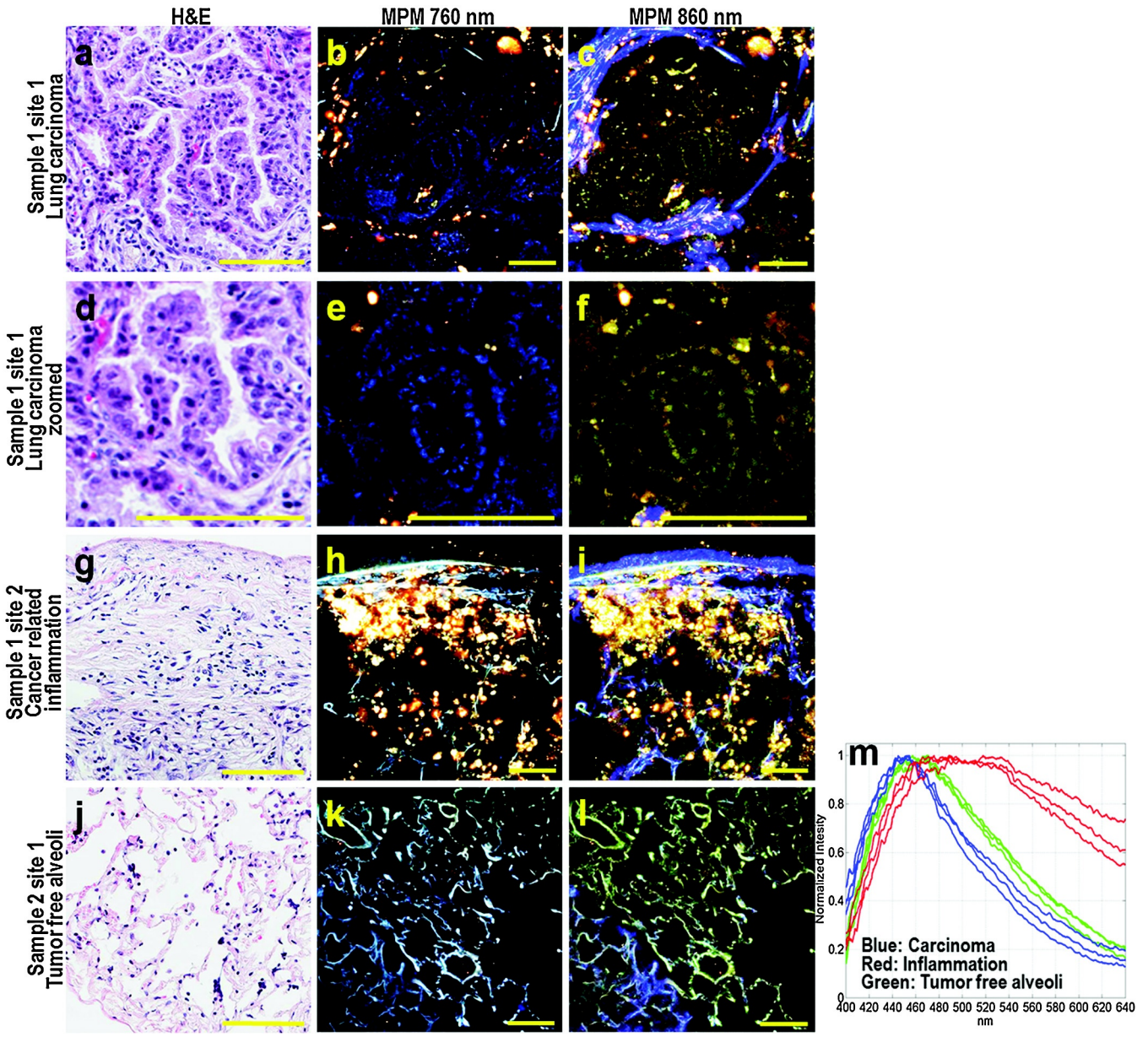

Fig. 6 Images from a resected canine lung lobe with naturally occurring bronchioloalveolar carcinoma before multiphoton microscopy (MPM) and after (H&E) tissue processing. (a–f), A site within the carcinoma displaying cellular papillary projections that compress the surrounding parenchyma. (g–i), A site histopathologically confirmed as infiltrates of inflammatory cells (macrophages and lymphocytes) associated with the tumor. (j–l), A site from an area of normal, tumor-free pulmonary parenchyma. (m), Two-photon excited fluorescence spectra at 760 nm excitation from cells within the carcinoma site (blue lines) and the cancer-associated inflammation site (red lines), and from intact alveoli in the tumor-free lung site (green lines). Scale bar: 100 μm.

MPM images [Figs. 6(b) and 6(e)] and displayed emission spectra with a peak at ~455 nm [Fig. 6(m), blue lines]. MPM images from another region within the abnormal sample displayed accumulation of cells with yellow appearance (fluorescence at 500 to 635 nm). This region was histopathologically confirmed as cancer-associated inflammation. At 760 nm excitation, emission spectra from these cells displayed a red-shifted fluorescence compared to cells within the carcinoma region [Fig. 6(m), red lines]. By comparison, MPM of tumor-free peripheral lung detected intact alveoli without readily visualized cellular component. These features were similar to MPM detected characteristics of mouse normal, inflammatory and malignant lung and suggest that the MPM detected characteristics of mouse neoplasms (Table 1) would be also valid for spontaneously occurring lung carcinomas in larger mammals.

4 Discussion

A preliminary step in evaluating MPM as a technique for early lung cancer detection requires studying the intrinsic two-photon excited fluorescence and SHG of lung and the selection of criteria from MPM images for lung nodules differentiation. We performed *ex vivo* MPM on unprocessed lung from mouse models of lung adenocarcinoma at differing stages of cancer development. Comparison of MPM and H&E images from the same region before and after tissue processing indicated that two-photon excited intrinsic fluorescence and SHG showed similar microanatomical information as standard histopathology. Detection of the two-photon excited fluorescence at three different emission regions also allowed visualizing the spectral characteristics of unprocessed normal and abnormal lung, not possible using standard histopathology. Our results have demonstrated that two-photon excited intrinsic fluorescence and SHG provide both structural and spectral contrast between normal, inflammatory, and neoplastic lung.

Structurally, mouse lung neoplasms are distinguished from tumor-free unaffected peripheral lung sites by an increased cellularity that is easily detected by MPM. Adenomas and adenocarcinomas appeared in MPM images as dense cellular masses that completely displaced the normal lung parenchyma. In contrast, the intrinsic fluorescence of tumor-free unaffected lung sites originated from intact alveoli without readily visualized cells (except for alveolar macrophages). These MPM-detected changes are in agreement with previous histological evaluation of mouse models of lung adenocarcinoma that characterize precursor lung lesions as an increased proliferation of cells along the alveolar septa that eventually form cellular masses, such as adenomas and adenocarcinomas.[25] A previous MPM study on frozen human lung adenocarcinoma samples[29] also detected increased cellularity in lung cancer nodules compared to unaffected peripheral lung. Our results demonstrate that MPM detects typical pathological changes in mouse lung microarchitecture caused by tumor progression without the need for tissue processing. *Ex vivo* label-free MPM of canine lung confirmed that similar microanatomical changes can also be observed in spontaneously occurring lung cancer in larger mammals.

Spectral data from MPM imaging demonstrated that mouse lung neoplasms have different intrinsic fluorescence compared to tumor-free unaffected lung. MPM at 760 nm excitation demonstrated that most cells within lung neoplasms displayed fluorescence detected predominantly at 420 to 460 nm. Two-photon excited emission spectra from cells within neoplasms peaked at ~455 nm, which is very similar to the emission peak wavelength of the cellular metabolic indicator, NADH.[12,17–18] In comparison, two-photon excited spectra from tumor-free unaffected mouse lung sites had a different peak (~480 nm, data not shown) and shape, suggesting a different origin of fluorescence. Therefore, MPM differentiated mouse adenomas and adenocarcinomas from tumor-free unaffected lung sites based on both structural (increased cellularity) and spectral (blue-shifted fluorescence) characteristics. This differentiation was observed in neoplastic and normal sites from two different mouse models and in resected canine lung tissue. This suggests that the described MPM characteristics are not particular to a specific lung cancer model and also would be valid for detecting spontaneously occurring lung carcinomas in larger mammals. We also showed that spectral MPM-detected characteristics differentiated benign from malignant neoplasms, an outcome not possible using only structural MPM-detected characteristics. Specifically, fluorescence emission ratio analysis of MPM images (and microspectroscopy) demonstrated that cells within adenomas displayed small spectral differences compared to cells within the malignancies. Together, these results demonstrate that MPM can be used as a microscopic technique to detect spectral, in addition to microanatomical, change in lung tissue with tumor progression.

MPM also demonstrated an increased cellularity with a distinct red-shifted fluorescence in mouse lung sites with diffuse or focal inflammation. As confirmed by histopathology, the cellular composition of these sites differed from that in tumors and consisted of inflammatory cells such as lymphocytes and/ or macrophages. MPM images from cancer related inflammatory sites from canine lung also showed cellular accumulations with red-shifted fluorescence compared to neoplastic cells. Porphyrin and lipofuscin, found in the vacuoles of macrophages, are fluorophores with dominant emission in the 505 to 655 nm range,[30] and are likely responsible for the observed red-shifted fluorescence of inflammatory sites. The presence of cellular red-shifted emission in cellular aggregates in respiratory lung could serve as a marker to distinguish inflammatory nodules from lung neoplasms. For example, granulomas, benign nodules in humans composed of inflammatory cells, are likely to have red-shifted fluorescence when examined by MPM compared to lung adenocarcinomas.

Two-photon excited microspectroscopy from cells within lung neoplasms and inflammatory lung sites confirmed spectral trends observed in the MPM images. In particular, two-photon excited fluorescence spectra from inflammatory sites exhibited a large red spectral broadening compared to spectra from lung tumor sites in both mouse and canine samples. Microspectroscopy measurements from mouse neoplasms also showed, similar to the quantitative analysis of MPM images, that cells within benign tumors exhibit small spectral broadening compared to cells within malignant tumors. While these microspectroscopy results need to be further validated on samples from spontaneously occurring lung cancers, we provided initial evidence that two-photon excitation microspectroscopy, in addition to imaging, detects spectral differences between neoplastic and inflammatory lung sites. Therefore, two-photon excited fluorescence microspectroscopy could also be used as a clinically relevant technique to sample regions of interest within lung nodules for the minimally invasive differentiation of inflammatory from neoplastic lung sites.

We have demonstrated the feasibility of using MPM as a microscopic technique for detecting inflammation and cancer related changes in *ex vivo* mouse and canine lung. We expect

that the described MPM-detected structural and spectral characteristics are also relevant for human lung, because the mouse models used in this study genetically and morphologically mimic human lung neoplasms. Results from the spontaneously occurring canine lung carcinoma further validated the relevance of the described MPM-detected characteristics for the minimally invasive imaging of lung neoplasms in larger mammals such as humans. Human lung tumors are usually diagnosed by sampling lung tissue with CT-guided needle biopsies and evaluating tissue samples by pulmonary cytology or histopathology. While this procedure yields accurate diagnosis for larger nodules, it has variable accuracy for small (<1 mm) and heterogeneous nodules. Additionally, it does not allow for direct, real-time assessment of the suspicious lesion. An endoscopic implementation of MPM to transthoracic (optical) needle biopsies or bronchoscopes would allow for the direct microscopic evaluation of nodules and possible real-time differentiation of benign from malignant lung sites. Fiber-coupled multiphoton endoscopes that detect intrinsic SHG from collagen and exogenous two-photon excited fluorescence from biological samples have already been reported.[31–33] Several groups have also concentrated on designing fiber-coupled multiphoton endoscopes for the efficient detection of intrinsic fluorescence from unprocessed tissue. While we demonstrate MPM-detected differentiation between lung abnormalities, successful *in vivo* application will depend partially on the design of a MPM endoscope offering optimized collection of the weak endogenous fluorescence from optically attenuating tissues, such as the lung.

Acknowledgments

We thank Cheryl Balkman for recruiting the canine patient for this study and for help in obtaining the canine lung samples. We also thank the members of the Histology Laboratory at the College of Veterinary Medicine, Cornell University, for technical support and H&E slide preparation. This research was supported by US National Institutes of Health grants CA108773 (RSW) and R01-EB006736 (IP and WWW). SAY was supported through a DOD Breast Cancer Research Program predoctoral fellowship, and KRH was supported through a Cornell University College of Veterinary Medicine Clinical Fellow Award. Editorial help from Mark Williams is greatly appreciated.

References

1. A. Jemal et al., "Cancer statistics," *CA Canc. J. Clin.* **60**(5), 277–300 (2010).
2. C. I. Henschke et al., "Early lung cancer action project: overall design and findings from baseline screening," *Lancet* **354**(9173), 99–105 (1999).
3. National Lung Screening Trial Research Team, "The national lung screening trial: overview and study design," *Radiology* **258**(1), 243–253 (2011).
4. K. Y. Lin et al., "In vivo quantitative microvasculature phenotype imaging of healthy and malignant tissues using a fiber-optic confocal laser microprobe," *Transl. Oncol.* **1**(2), 84–94 (2008).
5. R. Kiesslich, M. Goetz, and M. F. Neurath, "Confocal laser endomicroscopy for gastrointestinal diseases," *Gastrointest. Endosc. Clin. N. Am.* **18**(3), 451–466 (2008).
6. N. Thekkek, S. Anandasabapathy, and R. Richards-Kortum, "Optical molecular imaging for detection of Barrett's-associated neoplasia," *World J. Gastroenterol.* **17**(1), 53–62 (2011).
7. M. Kobayashi et al., "Detection of early gastric cancer by a real-time autofluorescence imaging system," *Canc. Lett.* **165**(2), 155–159 (2001).
8. S. Lam et al., "Detection and localization of early lung cancer by fluorescence bronchoscopy," *Cancer* **89**(11 suppl), 2468–2473 (2000).
9. L. Thiberville et al., "Confocal fluorescence endomicroscopy of the human airways," *Proc. Am. Thorac. Soc.* **6**(5), 444–449 (2009).
10. W. Denk, J. H. Strickler, and W. W. Webb, "Two-photon laser scanning fluorescence microscopy," *Science* **248**(4951), 73–76 (1990).
11. W. R. Zipfel, R. M. Williams, and W. W. Webb, "Nonlinear magic: multiphoton microscopy in the biosciences," *Nat. Biotechnol.* **21**(11), 1369–1377 (2003).
12. W. R. Zipfel et al., "Live tissue intrinsic emission microscopy using multiphoton excited intrinsic fluorescence and second harmonic generation," *Proc. Natl. Acad. Sci. USA* **100**(12), 7075–7080 (2003).
13. S. Mukherjee et al., "Human bladder cancer diagnosis using multiphoton microscopy," *Proc. SPIE* **7161**, 716117 (2009).
14. R. M. Williams et al., "Strategies for high-resolution imaging of epithelial ovarian cancer by laparoscopic nonlinear microscopy," *Transl. Oncol.* **3**(3), 181–194 (2010).
15. J. N. Rogart et al., "Multiphoton imaging can be used for microscopic examination of intact human gastrointestinal mucosa ex vivo," *Clin. Gastroenterol. Hepatol.* **6**(1), 95–101 (2008).
16. A. K. Tewari et al., "Multiphoton microscopy for structure identification in human prostate and periprostatic tissue: implications in prostate cancer surgery," *BJU Int.* **108**(9), 1421–1429 (2011).
17. Q. Yu and A. A. Heikal, "Two-photon autofluorescence dynamics imaging reveals sensitivity of intracellular NADH concentration and conformation to cell physiology at the single-cell level," *J. Photochem. Photobiol. B* **95**(1), 46–57 (2009).
18. H. D. Vishwasrao et al., "Conformational dependence of intracellular NADH on metabolic state revealed by associated fluorescence anisotropy," *J. Biol. Chem.* **280**(26), 25119–25126 (2005).
19. X. Han et al., "Second harmonic properties of tumor collagen: determining the structural relationship between reactive stroma and healthy stroma," *Opt. Express* **16**(3), 1846–1859 (2008).
20. B. Young et al., *Weather's Functional Histology: A Text and Color Atlas*, 5th ed., Churchill Livingstone/Elsevier, Philadelphia, PA, pp. 242–246 (2006).
21. T. Abraham and J. Hogg, "Extracellular matrix remodeling of lung alveolar walls in three dimensional space identified using second harmonic generation and multiphoton excitation fluorescence," *J. Struct. Biol.* **171**(2), 189–196 (2010).
22. A. M. Pena et al., "Three-dimensional investigation and scoring of extracellular matrix remodeling during lung fibrosis using multiphoton microscopy," *Microsc. Res. Tech.* **70**(2), 162–170 (2007).
23. K. M. Kerr, "Pulmonary preinvasive neoplasia," *J. Clin. Pathol.* **54**(4), 257–271 (2001).
24. V. Kumar et al., *Pathological Basis of Disease*, 8th ed., Saunders/Elsevier, Philadelphia, PA, pp. 724–726(2010).
25. E. L. Jackson et al., "Analysis of lung tumor initiation and progression using conditional expression of oncogenic K-ras," *Genes Dev.* **15**(24), 3243–3248 (2001).
26. X. Xu et al., "Broad overexpression of ribonucleotide reductase genes in mice specifically induces lung neoplasms," *Canc. Res.* **68**(8), 2652–2660 (2008).
27. A. Y. Nikitin et al., "Classification of proliferative pulmonary lesions of the mouse: recommendations of the mouse models of human cancers consortium," *Canc. Res.* **64**(7), 2307–2316 (2004).
28. E. L. Jackson et al., "The differential effects of mutant p53 alleles on advanced murine lung cancer," *Canc. Res.* **65**(22), 10280–10288 (2005).
29. C. C. Wang et al., "Differentiation of normal and cancerous lung tissues by multiphoton imaging," *J. Biomed. Opt.* **14**(4), 044034 (2009).
30. R. Richards-Kortum and E. Sevick-Muraca, "Quantitative optical spectroscopy for tissue diagnosis," *Annu. Rev. Phys. Chem.* **47**, 555–606 (1996).
31. L. Fu et al., "Nonlinear optical endoscopy based on a double-clad photonic crystal fiber and a MEMS mirror," *Opt. Express* **14**(3), 1027–1032 (2006).
32. Y. Wu et al., "Scanning all-fiber-optic endomicroscopy system for 3D nonlinear optical imaging of biological tissues," *Opt. Express* **17**(10), 7907–7915 (2009).
33. S. Tang et al., "Design and implementation of fiber-based multiphoton endoscopy with microelectromechanical systems scanning," *J. Biomed. Opt.* **14**(3), 034005 (2009).